JPE 18-2-8

https://doi.org/10.6113/JPE.2018.18.2.395
ISSN(Print): 1598-2092 / ISSN(Online): 2093-4718

Clamping-diode Circuit for Marine Controlled-source Electromagnetic Transmitters

Hongxi Song†, Yiming Zhang*, Junxia Gao*, Yu Zhang*, and Xinyue Feng*

†,* Faculty of Information Technology, Beijing University of Technology, Beijing, China

Abstract

Marine controlled-source electromagnetic transmitters (MCSETs) are important in marine electromagnetic exploration systems. They play a crucial role in the exploration of solid mineral resources, marine oil, and gas and in marine engineering evaluation. A DC–DC controlled-source circuit is typically used in traditional MCSETs, but using this circuit in MCSETs causes several problems, such as large voltage ringing of the high-frequency diode, heating of the insulated-gate bipolar transistor (IGBT) module, high temperature of the high-frequency transformer, loss of the duty cycle, and low transmission efficiency of the controlled-source circuit. This paper presents a clamping-diode circuit for MCSET (CDC-MCSET). Clamping diodes are added to the controlled-source circuit to reduce the loss of the duty ratio and the voltage peak of the high-frequency diode. The temperature of the high-frequency diode, IGBT module, and transformer is decreased, and the service life of these devices is prolonged. The power transmission efficiency of the controlled-source circuit is also improved. Saber simulation and a 20 KW MCSET are used to verify the correctness and effectiveness of the proposed CDC-MCSET.

Key words: Clamping-diode circuit, Converter efficiency, DC–DC controlled-source circuit, Marine controlled-source electromagnetic transmitter

I. INTRODUCTION

Marine controlled-source electromagnetic detection is an effective method for marine resource exploration, and marine controlled-source electromagnetic transmitters (MCSETs) are the core equipment of marine electromagnetic detection systems [1]. Marine controlled-source electromagnetic detection can identify high-resistivity reservoirs and can thus increase the drilling success rate. Many international oil and marine geophysical exploration companies are pursuing marine electromagnetic exploration in major sea areas of the world [2]. Marine electromagnetic detection systems possess many problems, such as large volume and mass, low efficiency, high heating, and low transient waveform. Therefore, they cannot meet actual exploration needs [3], [4]. An electromagnetic sounding transmitter towed by tugs is utilized in electromagnetic sounding systems to stimulate electromagnetic waves in the sea. A multi-component electromagnetic receiver is placed at the bottom of the sea to measure the electromagnetic field value by calculating the apparent resistivity and phase. The distribution pattern of the marine bottom structure and mineral resources is then revealed [5]-[7].

A zero-voltage-zero-current switching (ZVZCS) full-bridge converter overcomes the limitations of zero-voltage switching (ZVS). The duty cycle loss is compensated for, a blocking capacitor is used in, and saturated inductance is added to the full-bridge converter. In addition, the leading switch achieves ZVS, and the lagging switch achieves zero-current switching (ZCS), thus verifying the correctness of the analysis in [8] and [15]. A resonant inductor and two clamping diodes are added in the phase-shifted full-bridge DC–DC converter to significantly reduce the loss of the IGBT tube and high-frequency diode. A large resonant inductor is utilized for the converter to achieve ZVS at light loads, but it easily causes duty cycle loss. Analyses and experimental verification were performed by [9], [10]. A phase-shifted full-bridge converter achieves ZVS due to the use of a resonant inductor and two clamping diodes, and voltage oscillation caused by the reverse recovery of the rectifier diode is eliminated. The

Manuscript received Sep. 18, 2017; accepted Nov. 27, 2017
Recommended for publication by Associate Editor Honnyong Cha.
†Corresponding Author: shxbill@163.com
Tel: +86-10-6739-6621, Fax: +86-10-6739-6621, Beijing Univ. of Tech.
*Faculty of Information Tech., Beijing University of Technology, China

© 2018 KIPE

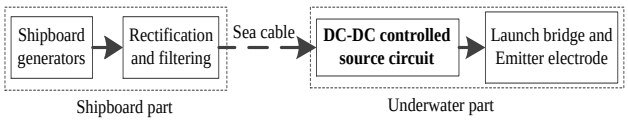

Fig. 1. Overall structural diagram of MCSET.

positions of the resonant inductor and transformer are changed to allow the transformer to be connected to the lagging switch; hence, improved efficiency and minimal duty cycle loss are achieved [11]. A clamping diode has also been used in a ZVS full-bridge converter to eliminate the voltage oscillation of the high-frequency diode. The conversion efficiency and reliability of the improved converter were increased. The principle of the improved converter was analyzed in detail in [12]. An improved full-bridge DC–DC converter was proposed in [13]. Two clamping diodes and two small coupling inductors were added to the primary side of the transformer, and ZVS was achieved within a wide load range. The working principle of the improved converter was analyzed to reduce the voltage ringing of the high-frequency diode.

As shown in Fig. 1, a marine transmitter can be divided into shipboard and underwater parts. The shipboard part mainly includes shipboard generators, a rectifier, and a filter circuit. The underwater parts include the pressure cabin, an underwater tow, a DC–DC controlled-source circuit, a launching bridge, and a launching electrode [14]. The shipboard generators provide initial electrical energy for the entire electromagnetic detection launching system, and the ship-borne generator AC voltage is converted to DC voltage by the rectifier and filter circuit to reduce the energy loss of the ship carrying the sea cable to the underwater transmitter. The shipboard underwater tow is used for the mechanical connection between the ship and pressure cabin. In addition, power and signal transmission are conducted simultaneously [15]. The electric energy is transmitted to the underwater pressure cabin from shipboard generators by sea cable. The DC–DC controlled-source circuit is mainly used to transfer the electric energy to the controlled DC. The controlled DC is converted to AC by the frequency-adjustable square wave. Electric energy is stimulated into the sea medium via a transmitting electrode [16]. The DC–DC controlled-source circuit is a key component of MCSET, and its performance and efficiency directly affect the performance of the entire MCSET.

II. CONTROLLED-SOURCE CIRCUIT

The traditional controlled-source circuit (T-CSC) is shown in Fig. 2. The waveform of T-CSC is shown in Fig. 3. The voltage ringing of the high-frequency diode is relatively large, and the voltage stress of the high-frequency diode is increased.

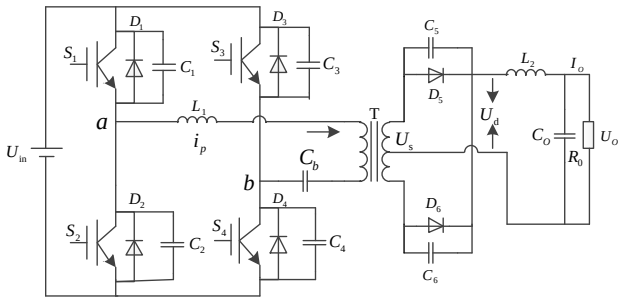

Fig. 2. Traditional controlled-source circuit.

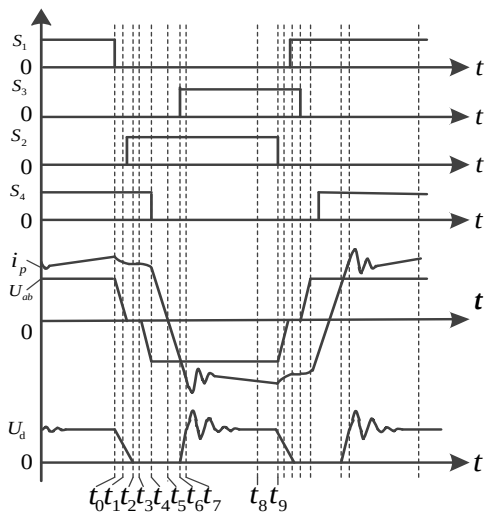

Fig. 3. Traditional controlled-source circuit waveform.

As shown in Fig. 4, the general method of suppressing the voltage spike of the high-frequency diode is through the use of an RC buffer circuit, an RCD buffer circuit, a passive lossless buffer circuit, an active clamp circuit, and a circuit for adding a clamp diode in the primary side of the transformer [17]-[19].

The RC buffer circuit is inexpensive and possesses a good absorption capability, as shown in Fig. 4(a). However, resistance R consumes energy and thus reduces the efficiency of the controlled-source circuit significantly. In Fig. 4(b), diode D is added, and the RCD buffer circuit is similar to the RC buffer circuit. The RCD buffer circuit returns the energy to the power source. Resistance R also consumes energy and reduces the efficiency of the controlled-source circuit. The parameters become complex and difficult to debug in high-power conditions. Fig. 4(c) shows an active clamp circuit that is expensive and requires control and drive circuits. Fig. 4(d) presents a passive, lossless buffer circuit with a large capacity, good inhibitory effect, and no power loss. However, the transformer overshoot of the current is large, and the need for additional devices results in high costs. Therefore, this circuit is unsuitable for high-power scenarios. The current work presents a clamping-diode circuit for MCSET (CDC-MCSET).

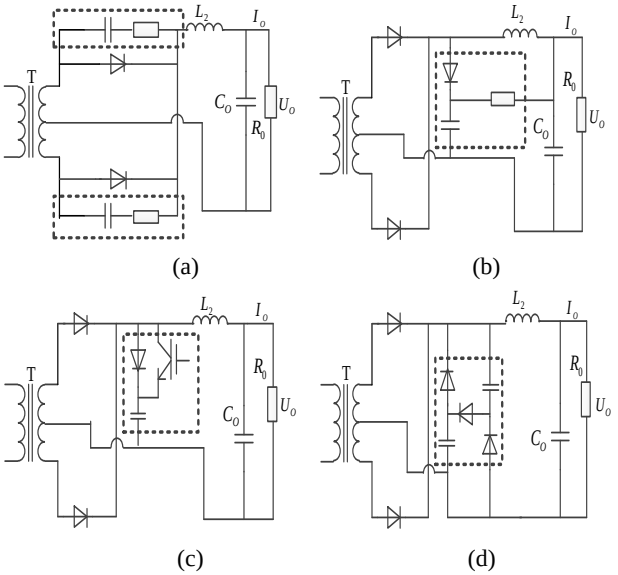

Fig. 4. Schematic of the buffer circuit.

III. Clamping-diode Circuit Structure and Working State Analysis

A. Clamping-Diode Controlled-Source Circuit Structure

This section analyzes the working principle of the clamping-diode controlled-source circuit (CD-CSC). As shown in Figs. 5 and 6, the controlled-source circuit is assumed to satisfy the following conditions.

a) All switch tubes, diodes, inductors, capacitors, and transformers are ideal components, except for the high-frequency diodes (D_5 and D_6).

b) C_1=C_2 =C_{12}, C_3=C_4= C_{34}, C_5=C_6= C_{56}.

c) The output filter capacitor (C_0) is sufficiently large.

B. Clamping-Diode Circuit Working State Analysis

As shown in Fig. 6, we analyze the 20 operating states of CD-CSC [9–12].

Switching mode 1, $t < t_0$.

According to the equivalent circuit model in Fig. 7(a), before t_0, S_1, S_4, and D_5 are all turned on, D_6 is turned off, and the primary energy of the transformer is transmitted to the transformer secondary side.

Switching mode 2, $t_0 < t < t_1$.

According to the equivalent circuit model in Fig. 7(b). At t_0, I_{t0} is the primary current of the transformer converted from the output current of the filter inductor. S_1 is turned off in the ZVS mode due to C_1 and C_2 buffers. The primary current i_p of the transformer is charged to C_1, and the C_2 discharge (U_{ab}) is decreased. The primary equivalent capacitance C_{56p} of the transformer is converted from C_{56}. When U_{ab} decreases, the primary voltage U_{cb} and secondary voltage U_s of the transformer decrease. Parasitic junction capacitor C_6 of high-frequency diode D_6 begins discharging.

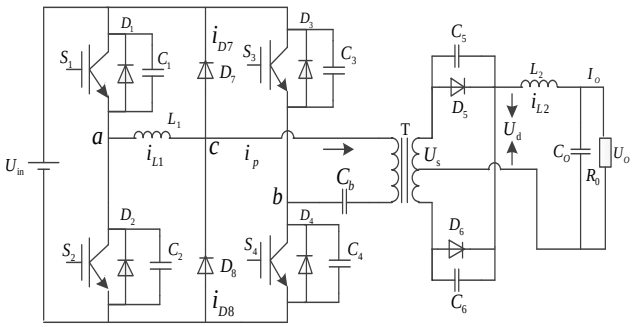

Fig. 5. Clamping-diode controlled-source circuit.

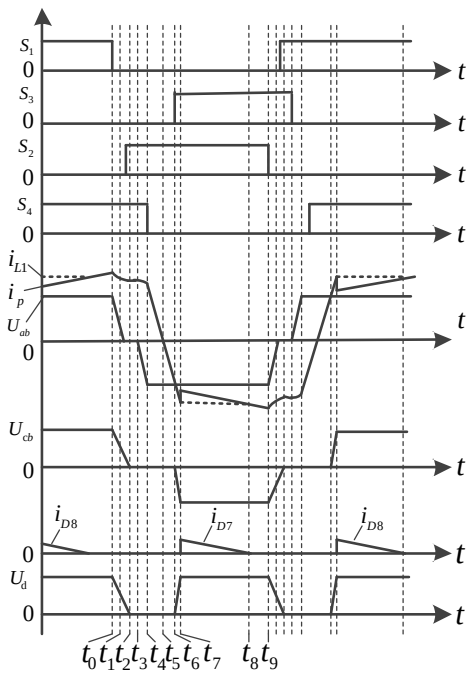

Fig. 6. Clamping-diode controlled-source circuit waveform.

At t_1, the voltage of C_1 rises to U_{in}. The voltage of C_2 decreases to zero, and D_2 is turned on. During $t_0 < t < t_1$, U_{C1} and U_{C2} can be approximated as

$$U_{C1}(t) = \frac{I_{t0}(t - t_0)}{2C_{12} + C_{56p}} \quad , \tag{1}$$

$$U_{C2}(t) = U_{in} - \frac{I_{t0}(t - t_0)}{2C_{12} + C_{56p}} \quad . \tag{2}$$

Switching mode 3, $t_1 < t < t_2$.

According to the equivalent circuit model in Fig. 7(c), after D_2 is turned on, S_2 is turned on in the ZVS mode. When the voltage of "a" is zero, the voltage of "c" is not zero. C_6 continues to be discharged, and i_{L1} and i_P continue to decrease. At t_1, I_{t1} is the primary current of the transformer. At t_2, C_6 is the discharged ends, D_6 is turned on, and the voltage of "c" drops to zero.

Switching mode 4, $t_2 < t < t_3$.

According to the equivalent circuit model in Fig. 7(d), D_5

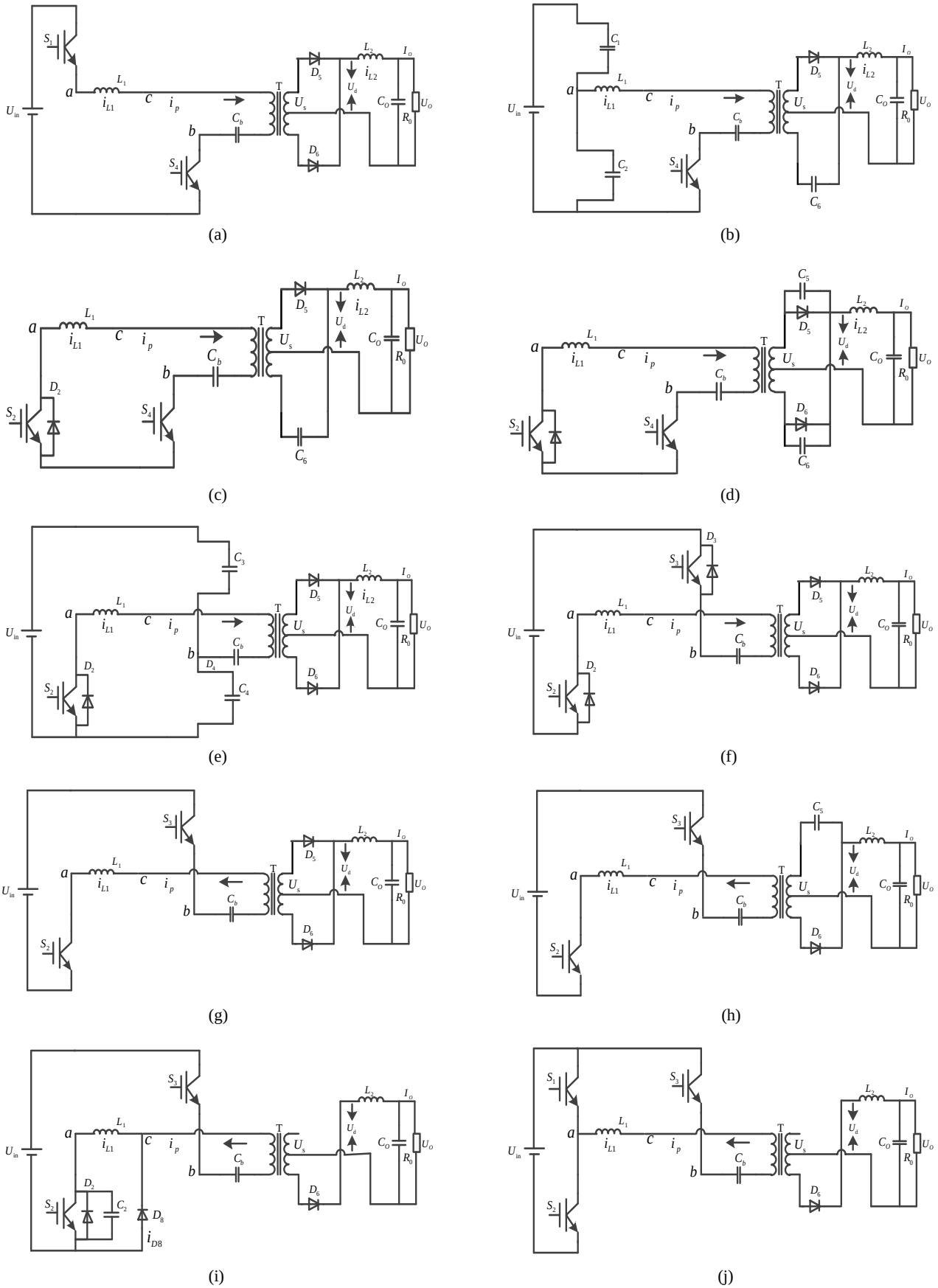

Fig. 7. Clamping-diode controlled-source equivalent circuit.

and D_6 are turned on, and the primary and secondary voltages of the transformer are clamped at zero. The voltage of "a", "b", and "c" are all zero, and i_{L1} and i_P are equal in the natural freewheeling state and remain unchanged.

Switching mode 5, $t_3 < t < t_4$.

According to the equivalent circuit model in Fig. 7(e), at t_3, S_4 is turned off in the ZVS mode due to C_3 and C_4 buffers. Current i_{L1} is charged to C_4 and discharged to C_3. D_5 and D_6 are turned on, the primary and secondary voltages of the transformer are zero, and the voltage of L_1 is U_{ab}. Thus, the resonance of C_3, C_4, and L_1 occurs at this time. At t_4, the voltage of C_4 rises to U_{in}, the voltage of C_3 drops to zero, and D_2 is turned off. U_{C3} and U_{C4} are presented as

$$U_{C4}(t) = Z_1 I_{t1} \sin \omega_1 (t - t_4) \quad , \tag{3}$$

$$U_{C3}(t) = U_{in} - Z_1 I_{t1} \sin \omega_1 (t - t_4) \quad , \tag{4}$$

$$Z_1 = \sqrt{L_1 / 2C_{34}} \quad , \tag{5}$$

$$\omega_1 = 1 / \sqrt{2 L_1 C_{34}} \quad . \tag{6}$$

Switching mode 6, $t_4 < t < t_5$.

According to the equivalent circuit model in Fig. 7(f), D_5 and D_6 continue to be turned on simultaneously, U_d=0, U_{cb}=0, the voltage of L_1 is $-U_{in}$, and i_{L1} and i_P decrease linearly. At t_5, i_{L1} and i_P drop to zero, and D_2 and D_3 are naturally turned off.

Switching mode 7, $t_5 < t < t_6$.

According to the equivalent circuit model in Fig. 7(g), from the start of t_5, i_{L1} and i_P are increased in the negative direction after crossing zero, and they flow through S_2 and S_3. Given that i_P is still insufficient to improve the load current, D_5 and D_6 continue to be turned on simultaneously, and U_d=0. The voltage of L_1 is $-U_{in}$, and i_{L1} and i_P decrease linearly. At t_6, i_P is presented as

$$i_p = - I_{L2}(t_6) / N = - I_o(t_6) / N \quad , \tag{7}$$

Where N is the ratio of the primary and secondary sides of the transformer. D_5 is turned off, and the output current of the filter inductor flows through D_6.

Switching mode 8, $t_6 < t < t_7$.

According to the equivalent circuit model in Fig. 7(h), from the start of t_6, the resonance of L_1 and C_5 occurs. Thus, i_{L1} and i_P continue to increase and are charged to C_4. At t_7, the voltage of C_5 increases to $2U_{in}/N$, whereas U_{cb} decreases to $-U_{in}$. Given that the voltage of "b" is U_{in}, the voltage of "c" decreases to zero, and clamping diode D_8 is turned on. U_{cb} is clamped at $-U_{in}$, and the voltage of C_5 is clamped at $i_p = -2U_{in}/N$. At this moment, i_{L1} and i_P are $-I_3$, which is as follows:

$$I_3 = \frac{I_{L2}(t_6)}{N} + \frac{U_{in}}{Z_3} \quad , \tag{8}$$

$$Z_3 = \sqrt{L_1 / C_{56p}} \quad . \tag{9}$$

Switching mode 9, $t_7 < t < t_8$.

According to the equivalent circuit model in Fig. 7(i), when D_8 is turned on, i_{L2} is converted to primary current i_P of the transformer. The formula $i_p = -i_{L2}/N$ is satisfied, and i_{L1} is I_3. It is unchanged and flows from D_8 with the difference from i_P. i_{L2} is increased linearly during this time, i_P is increased linearly with the reverse, and the current of D_8 is decreased linearly. At t_8, $i_{L1} = i_P$, and D_8 is turned off.

Switching mode 10, $t_8 < t < t_9$.

According to the equivalent circuit model in Fig. 7(j), the primary energy of the transformer is transmitted to the transformer secondary side, where $i_{L1} = i_P$.

$$i_p(t) = - \frac{U_{in} - N U_o}{N^2 L_2} (t - t_9) \tag{10}$$

The controlled-source circuit begins in the other half of the cycle, where the working condition is similar to the previous half cycle $t_0 < t < t_9$.

IV. Characteristic Analysis of the Controlled-source Circuit

A. Duty Cycle Loss of the Transformer Secondary Side

The duty cycle loss of the transformer secondary side is a problem in the controlled-source circuit. The duty cycle of the transformer secondary side is less than that of the primary side, and the difference is lost due to the existence of resonant inductance [20], [21]. The period of the primary current i_p conversion is $t_2 < t < t_7$. The primary current is insufficient to provide the load current, and the high-frequency diode is continuously turned on. The transformer secondary side is short-circuited, and voltage U_d is zero at t_3. I_{t3} is the primary current.

$$D_e = D - D_{loss} \tag{11}$$

$$\frac{U_o}{U_{in}} = N D_e \tag{12}$$

$$I_{t0} = N \left[I_o - \frac{\Delta I}{2} \right] \tag{13}$$

$$I_{t3} = N \left[I_o + \frac{\Delta I}{2} - (1 - D) \frac{U_o T}{2 L_1} \right] \tag{14}$$

$$D_{loss} = \frac{I_{t0} + I_{t3}}{\frac{U_{in}}{L_1} \frac{T}{2}} = \frac{2 N L_r}{U_{in} T} \left[2 I_o \frac{U_o}{L_1} (1 - D) \frac{T}{2} \right] \tag{15}$$

Equations (13) and (14) are provided in Equation (15).

$$D_{loss} = \frac{4 N L_1 I_o f_o - N U_o \frac{L_1}{L_2} + \frac{U_o^2}{U_{in}} \frac{L_1}{L_2}}{U_{in} - N U_o \frac{L_1}{L_2}} \approx \frac{4 N L_1 I_{L2}}{U_{in}} \tag{16}$$

In the equations above, D_e is the effective duty cycle, D_{loss} is the duty loss, I_o is the load current, and f_o is the switching

frequency. L_1, N, I_{L2}, and D_{loss} are proportional in Equation (16) but inversely proportional to U_{in}. To satisfy the requirements of MCSET design, input voltage U_{in}, the ratio of transformer N, and load current I_o are unchanged. To increase D_e, D_{loss} must be reduced so that resonant inductance L_1 is appropriately reduced.

B. ZVS

The function of the leading and lagging switches in this work is consistent with that in [11]. The two switches achieve ZVS in the controlled-source circuit. However, the function of the lagging switch in [8] and [15] is inconsistent with that in the current work. The leading switch achieves ZVS, filter inductor L_2 and resonant inductor L_1 are connected in series, and these two inductors store a sufficient value for energy E_1. Energy E_1 is charged to the parallel capacitance of the IGBT tube and is discharged to the parallel capacitance of IGBT on the same bridge arm. The two inductors are also used for the distributed capacitance of the transformer to release energy due to the existence of a distributed capacitor C_T in the high-frequency transformer windings. The distributed capacitance of the transformer is mainly divided into four parts: turn–to–turn, interlayer, winding, and stray capacitance. Interlayer capacitance is the main distributed capacitance of the transformer and exerts an important effect on the transformer in Fig. 8. When the IGBT is turned on and off, interlayer capacitor C_T resonates with the leakage inductance of the high-frequency transformer, which causes the peak voltage of the transformer. The voltage stress of the IGBT and the high-frequency diode is increased [21–23].

The energy E_1 satisfaction formula is

$$E_1 = \frac{1}{2}L_1 I_{L1}^2 + \frac{1}{2}L_2 I_{L2}^2 > C_{12}U_{in}^2 + \frac{1}{2}C_T U_{in}^2 \quad . \tag{17}$$

When the lagging switch is turned on, the primary voltage of the transformer is short-circuited. On the one hand, the primary current gradually converts the flow direction. On the other hand, the high-frequency diode is freewheeling for filter inductance. The primary energy of the transformer is transmitted to the transformer secondary side. Energy E_2 of the lagging switch achieving ZVS is only provided by resonant inductor L_1. Therefore, the lagging switch cannot easily implement ZVS. The energy E_2 satisfaction formula is

$$E_2 = \frac{1}{2}L_1 I_{L1}^2 > C_{34}U_{in}^2 + \frac{1}{2}C_T U_{in}^2 \quad . \tag{18}$$

When $I_{t3} = I_{L1}$, Equation (14) is substituted into Equation (18).

$$I_{L2} = I_o > \frac{U_{in}}{N}\sqrt{\frac{2}{L_1}\left(C_{34} + \frac{1}{2}C_T\right)} + (1-D)\frac{U_o T}{2L_2} - \frac{\Delta I}{2} \tag{19}$$

The realization of ZVS involves changing the two parameters in Equation (19). Primary current i_{L1} and resonant inductance L_1 are appropriately increased.

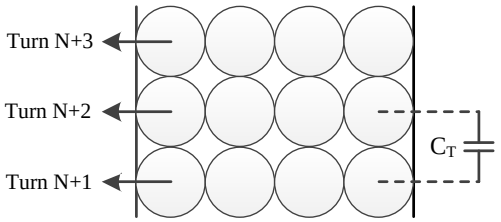

Fig. 8. Transformer interlayer equivalent capacitance.

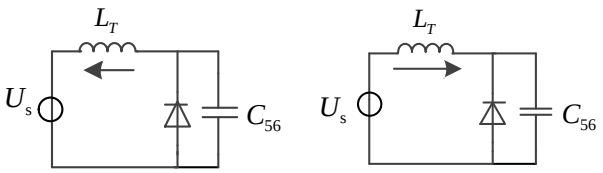

Fig. 9. High-frequency diode equivalent circuit. (a) Diode forward-conduction equivalent circuit. (b) Diode reverse-blocking equivalent circuit.

C. High-Frequency Diode Ringing

Parasitic capacitances exist in the high-frequency diodes in the controlled-source circuit. The flow direction of the primary current is gradually changed, and the transformer leakage inductance resonates with the parasitic capacitance of the high-frequency diode. The high-frequency diode produces a relatively high reverse voltage surge, which leads to significant heating, high temperature, and reduced service life. An equivalent model of transformer leakage inductance and high-frequency diode parasitic capacitance was established in [22]-[24] and is shown in Fig. 9.

The forward current of the high-frequency diode is i_{L2}. When the voltage of the high-frequency diode is $-U_s$, the diode begins reverse recovery. Current i_{LT} is increased from zero to reverse due to the leakage inductance of the transformer. Thus, the charge stored in the PN junction of the high-frequency diode is eliminated. After storing the charge, the reverse recovery current reaches the maximum I_{max}. The voltage of capacitor C_{56} increases from zero, the high-frequency diode reaches the blocking state and is infinite (R_∞), and the transformer leakage inductance resonates with the high-frequency diode parasitic capacitance.

The following formulas are established.

$$L_T \frac{di_{L2}}{dt} + U_{C56} = U_s \tag{20}$$

$$i_{LT} = C_{56}\frac{dU_{C56}}{dt} + \frac{U_{C56}}{R_\infty} \tag{21}$$

The initial value of these equations is

$$i_{LT}(0) = I_{\max} \quad , \tag{22}$$

$$U_{C56}(0) = 0 \quad . \tag{23}$$

We obtain

$$L_T C_{56}\frac{d^2U_{C56}}{dt^2} + \left(\frac{L_T}{R_\infty}\right)\frac{dU_{C56}}{dt} + U_{C56} = U_s \tag{24}$$

and

$$U_{C56} = U_A e^{-a_4 t}\sin(\omega_4 t - \varphi_4) + U_s \quad , \tag{25}$$

$$\begin{aligned} i_{LT} = {} & \frac{U_A}{R_\infty} e^{-a_4 t}\sin(\omega_4 t - \varphi_4) \\ & + \frac{U_s}{R_\infty} - a_4 C_{56} U_A e^{-a_4 t}\sin(\omega_4 t - \varphi_4) \\ & + \omega_4 C_{56} U_A e^{-a_4 t}\cos(\omega_4 t - \varphi_4) \end{aligned} \quad , \tag{26}$$

$$\varphi_4 = \tan^{-1}\frac{U_s}{(a_4/\omega_4)(2R_\infty I_{\max} - U_s)} \quad , \tag{27}$$

$$a_4 = \frac{1}{2R_\infty I_{\max}} \quad . \tag{28}$$

The oscillation frequency ω_4 and the voltage peak of the diode U_P are

$$U_P = \sqrt{U_s + (a_4/\omega_4)^2 (2R_\infty I_{\max} - U_s)^2} \quad , \tag{29}$$

$$\omega_4 = \frac{1}{\sqrt{L_T C_{56}}}\sqrt{1 - \left(\frac{\sqrt{L_T/C_{56}}}{2R_\infty}\right)} \quad , \tag{30}$$

$$R_\infty \geq \frac{1}{2}\sqrt{L_T/C_{56}} \quad . \tag{31}$$

If the leakage inductance of the transformer is reduced, according to Equations (29) and (31), voltage spike U_P will be reduced when a_4/ω_4 is reduced. If the diode parasitic capacitance is increased, according to Equations (29) and (31), voltage spike U_P will be reduced when a_4/ω_4 is reduced. This scenario allows for high-voltage or current applications where high-frequency diode oscillation is serious. Therefore, the high-frequency diode with suitable parasitic capacitance is selected to reduce the leakage inductance of the transformer and obtain a relatively low inductance spike.

According to Equations (16), (19), (29), and (31), the working state of the clamping-diode circuit is analyzed. On the one hand, to reduce D_{loss} and voltage spike U_P, resonant inductance L_1 must be small; on the other hand, to achieve ZVS, resonant inductance L_1 must be large. To meet the requirements of the MCSET indicator, the clamping diode is used to suppress voltage spike U_P, which increases the selection range of the inductor. Obtaining the appropriate saturated resonant inductor in an actual project is easy. The controlled-source circuit is tested repeatedly to identify the optimum saturated inductance.

V. Experimental Verification

Saber simulation and physical verification are used in the experiments to verify the correctness and validity of the analysis and theory. The parameters of the controlled-source circuit are shown in Table I.

A. Saber Simulation

Fig. 10 shows the phase-shifted driving waveforms of four IGBT tubes in the controlled-source circuit. The transformer

TABLE I

Parameters of the Controlled-Source Circuit

Parameters	Values
Input voltage(U_{in})	710V
Output voltage(U_0)	100V
Absorption Capacitance(C_1=C_2=C_3=C_4)	0.47uF
Switching frequency(f_o)	20kHz
Blocking capacitor(C_b)	20μF
Resonant inductance(L_r)	10μH
Ratio of the primary and secondary sides of the transformer(N)	5:1
Filter inductance(L_1=L_2)	47uH
Filter capacitor(C_0)	1500uF
Load(R_0)	0.5 Ω
Output current(I_o)	200A

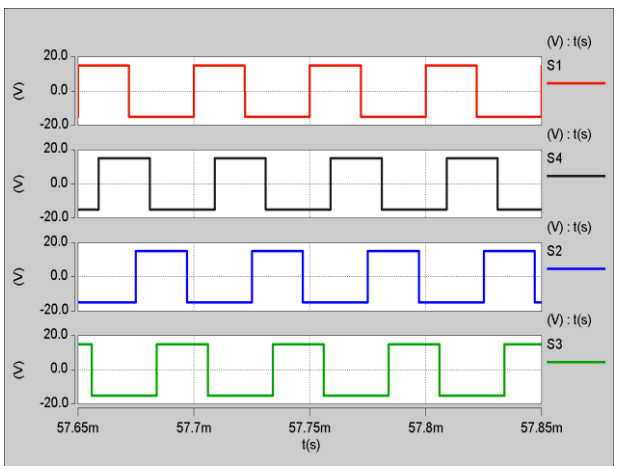

Fig. 10. Drive simulation waveforms of S_1, S_2, S_3, and S_4 IGBT tubes.

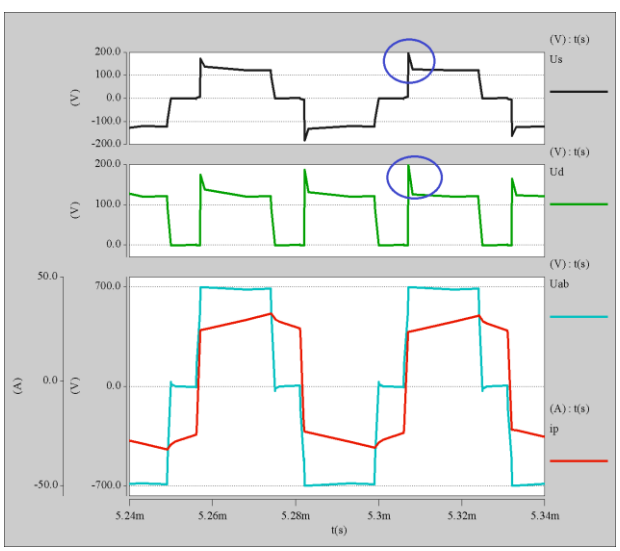

Fig. 11. T-CSC simulation waveform. U_s is the secondary voltage waveform of the transformer, U_d is the high-frequency diode output voltage waveform, U_{ab} is the primary voltage waveform of the transformer between "a" and "b," and i_P is the primary voltage waveform of the transformer.

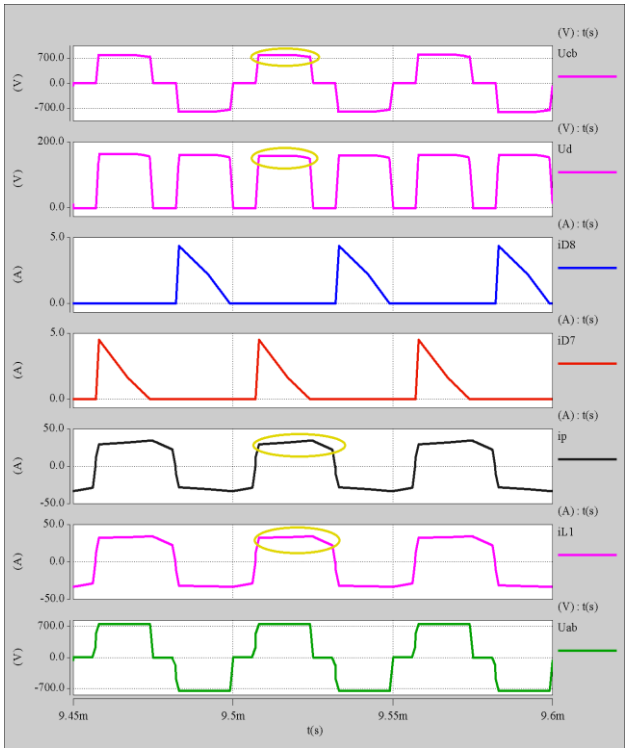

Fig. 12. CD-CSC waveform. U_{ab} is the primary voltage waveform of the transformer between "c" and "b", U_d is the high-frequency diode output voltage waveform, i_{D7} is the diode D_7 current, i_{D8} is the diode D_8 current, i_p is the primary current waveform of the transformer, i_{L1} is the resonant inductor L_1 current, and U_{ab} is the primary voltage waveform of the transformer between "a" and "b."

leakage inductance resonates with high-frequency diode parasitic capacitance. The high-frequency diode and the transformer secondary side cause voltage oscillation and spikes from the blue oval in Fig. 11. The voltage stress of the high-frequency diode and the transformer heat are increased. The output voltage U_d waveform of the high-frequency diode is clamped by the clamping diode, and it does not show voltage oscillation and spikes from the yellow oval in Fig. 12. The clamping diode can reduce the voltage peak of the high-frequency diode. The flow direction of the primary current is changed gradually, and resonant inductor i_{L1} is slightly higher than primary current i_P of the transformer. When the currents of the clamping diodes D_7 and D_8 are stopped, the currents of i_P and i_{L1} begin to converge again. This is basically similar to the CD-CSC waveform analysis.

B. Physical Verification

A 20 KW MCSET is used to verify the proposed method. As shown in Fig. 13, the IGBT module consists of A and B modules. The laboratory temperature is 15 ℃.

The experimental waveform in Figs. 14 and 15 shows that the physical waveforms of T-MCSET and CDC-MCSET are basically similar to the simulation waveform. According to Fig. 15(b), clamping diode currents i_{D7} and i_{D8} have nearly the same waveform. However, they are slightly different because the control circuit and internal parameters of the device are

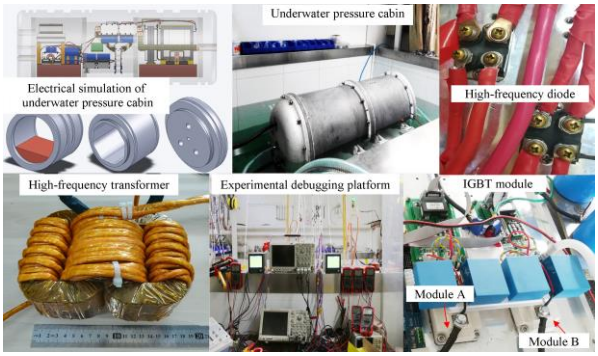

Fig. 13. MCSET physical diagram.

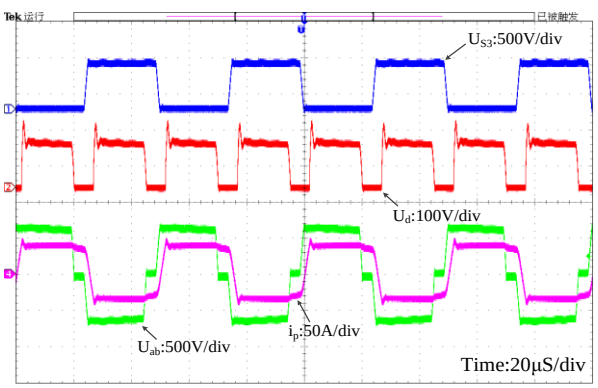

Fig. 14. T-MCSET physical waveform. U_d is the high-frequency diode voltage, U_{S3} is voltage waveform of the lagging switch S_3, U_{ab} is the primary voltage waveform of the transformer, and i_P is the primary current waveform of the transformer.

not completely consistent. This condition does not affect the experimental results. We further verify the feasibility and effectiveness of CDC-MCSET. The external temperature curve of the transformer, high-frequency diode, and IGBT module is shown below.

The temperature curve is shown in Fig. 16. When the transmitter continues its operation for five hours, the temperatures of the transformer, high-frequency diodes, and IGBT modules gradually increase with time. When the transmitter is in 3.5 hours of operation, the temperature of the T-MCSET transformer rises to 62 ℃ in Fig. 16(a). However, the temperature of the CDC-MCSET transformer rises to 50 ℃ in Fig. 16(b), and the temperatures present a stable trend. High-frequency diode D_5 is a blue curve, and D_6 is a red curve. In Figs. 16(c) and 16(d), when the transmitter is operated for 2.5 hours, the temperature of the T-MCSET high-frequency diode increases to 36 ℃. In Fig. 16(c), the temperature of the CDC-MCSET high-frequency diode increases to 32 ℃. As shown in Fig. 16(d), all temperatures are stable. Module A is a blue curve, and module B is a red curve in Figs. 16(e) and 16(f). When the transmitter is operated for an hour, the temperature of the T-MCSET IGBT module rises to 42 ℃ in Fig. 16(e). However, the temperature of the CDC-MCSET IGBT module rises to 37 ℃ in Fig. 16(f), and all temperatures are stable.

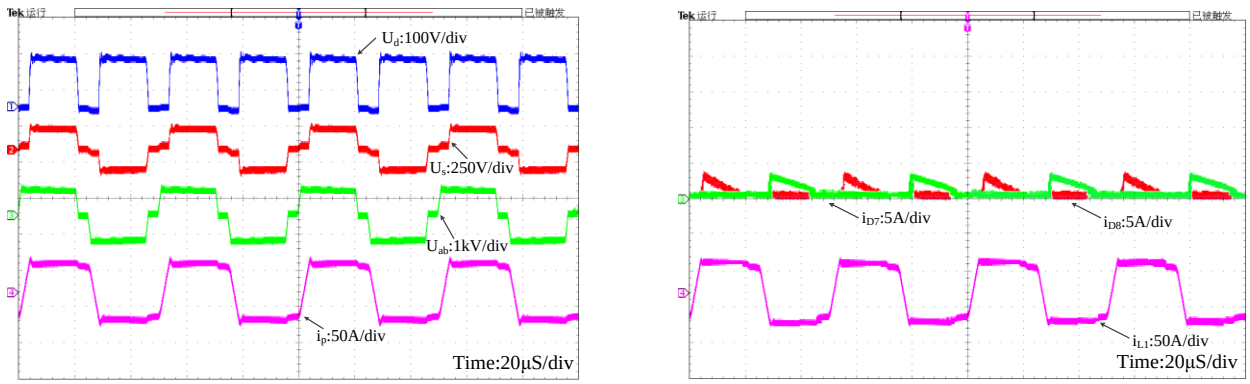

(a) (b)

Fig. 15. CDC-MCSET physical waveform. (a) U_d is the high-frequency diode output voltage waveform, U_s is the secondary voltage waveform of the transformer, U_{ab} is the primary voltage waveform of the transformer between "a" and "b", and i_p is the primary current waveform of the transformer. (b) i_{D7} is the diode D_7 current, i_{D8} is the diode D_8 current, and i_{L1} is the resonant inductor L_1 current.

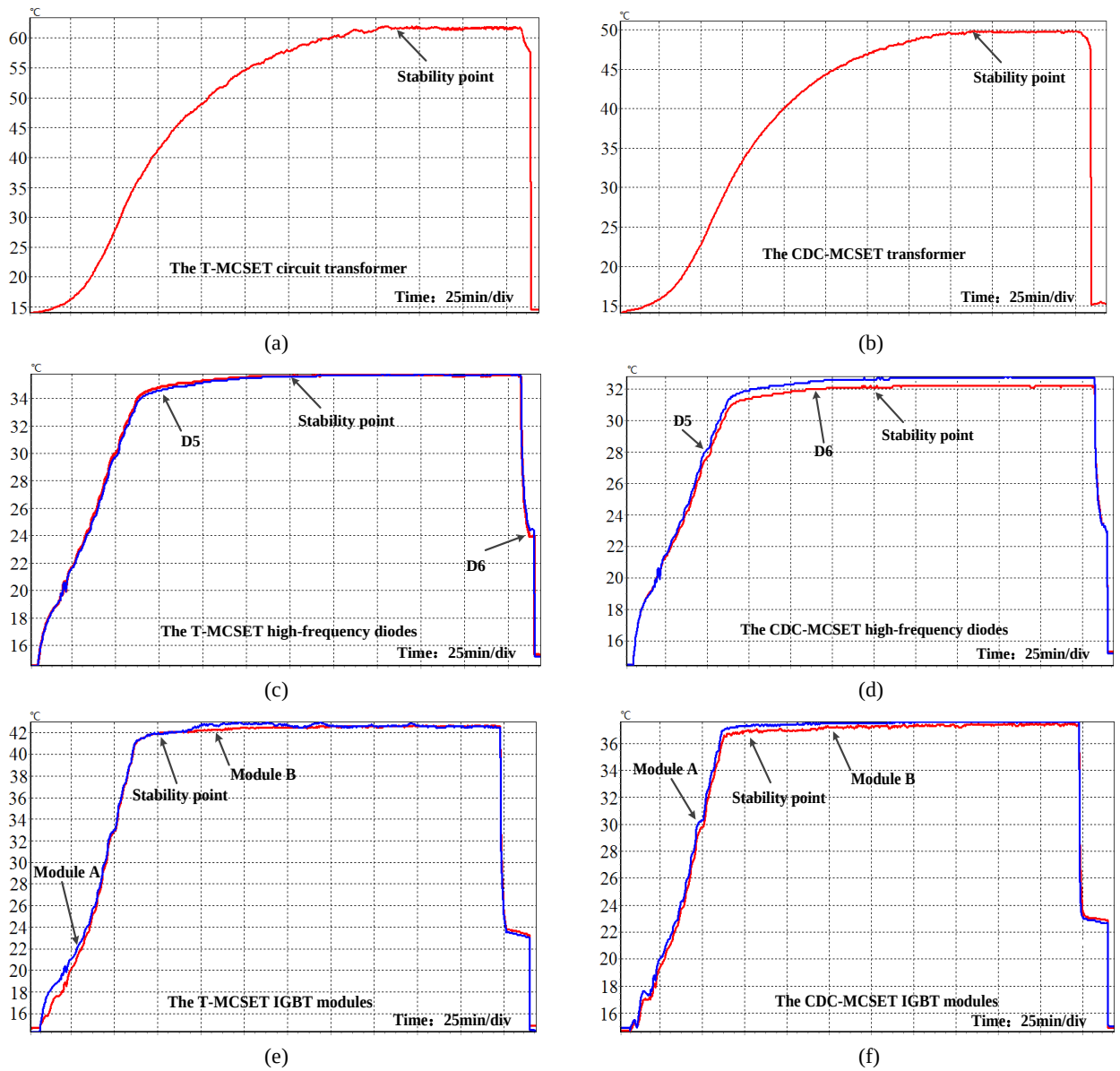

(a) (b) (c) (d) (e) (f)

Fig. 16. Temperature curve of the MCSET key components.

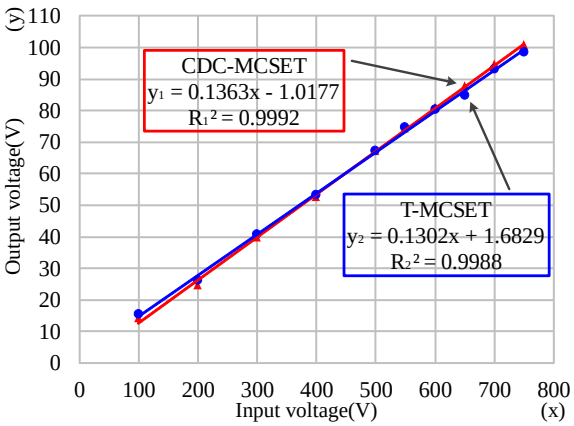

Fig. 17. Comparison of output voltage U_o and input voltage $U_{in.}$

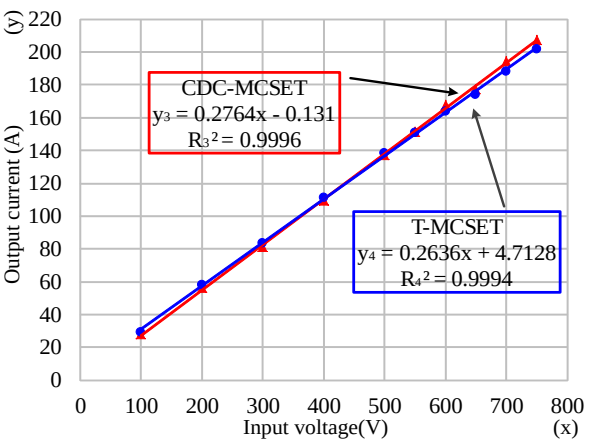

Fig. 18. Comparison of output current I_o and input voltage $U_{in.}$

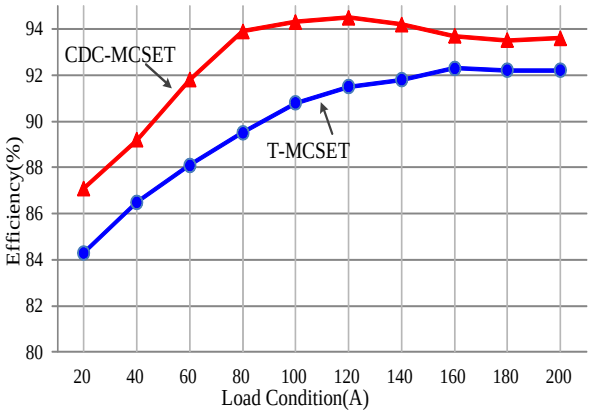

Fig. 19. Comparison of efficiency and load current.

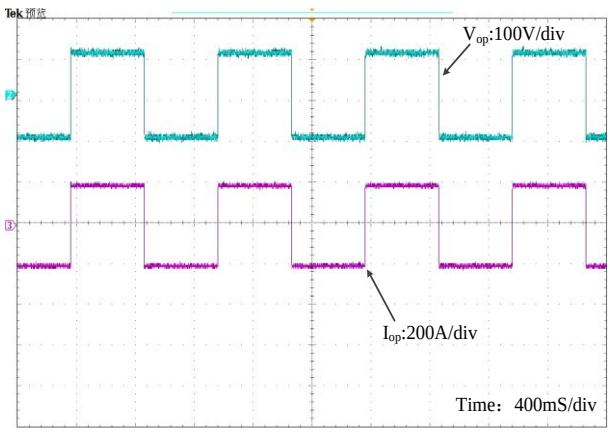

Fig. 20. CDC-MCSET emitting the voltage waveform V_{op} and the current waveform $I_{op.}$

According to the above analysis of CDC-MCSET, the primary and secondary currents of the transformer and the primary voltage spike of the transformer are decreased, and the temperature, conduction loss, heating capacity, and damage rate of the key components are reduced. The service life of the components is thus extended, and the conversion efficiency of the controlled-source circuit is improved.

In Figs. 17 and 18, the blue curve represents T-MCSET, and the red curve represents CDC-MCSET. Measurements are performed on the external characteristics of the controlled-source circuit in Figs. 17 and 18, and the two fitting curves and expressions of the controlled-source circuits are provided. The fitting coefficient R^2 is relatively high and close to 1. The output voltage is almost linearly proportional to the input voltage in Fig. 17, and the output current is also almost linearly proportional to the input voltage in Fig. 18. R_3^2 is slightly larger than R_4^2 because R_1^2 is slightly larger than R_2^2. Therefore, the external characteristics of CDC-MCSET are better than those of T-MCSET.

In Fig. 19, the blue curve represents T-MCSET, and the red curve represents CDC-MCSET. The conversion efficiency of CDC-MCSET is improved, and its speed increases as the load current is increased (maximum efficiency over 94%). However, when the load current is increased, the input voltage increases, the IGBT tube conduction presents a large loss, and efficiency is slightly decreased. When the full load current is 200 A, the efficiency of CDC-MCSET exceeds 93%. The overall efficiency of CDC-MCSET is obviously superior to that of T-MCSET.

According to Fig. 20, the CDC-MCSET is used to emit a square waveform, where voltage V_{op} is 100 V and current I_{op} is 200 A at 1 Hz. The two waveforms are almost synchronous. The rising and falling edges of voltage and current exhibit good steepness, strong stability, good linearity, and high controllability, which further prove the feasibility and effectiveness of CDC-MCSET.

VI. Conclusion

a) We develop a CDC-MCSET and analyze the various modes in the operating cycle of the CD-CSC. The transformer leakage inductance resonates with the high-frequency diode parasitic junction capacitance, resulting in high-frequency diode voltage spikes. The voltage stress is increased, and the clamping diode is clamped on the primary

side of the transformer to suppress the voltage ringing of the high-frequency diode.

b) The duty cycle loss of the transformer secondary side and the ZVS of the IGBT tube are analyzed. The expression of the ZVS condition is provided, and the corresponding formula is deduced. The appropriate saturated inductance is selected to reduce the duty cycle loss and obtain high conversion efficiency. Moreover, a circuit model of transformer leakage inductance and parasitic capacitance of the high-frequency diode is established. A small leakage inductance of the transformer and a large diode parasitic capacitance are beneficial to suppressing the voltage ringing of the high-frequency diode.

c) In the same condition, a temperature recorder is effectively used to record the temperature of the transformer, high-frequency diode, and IGBT module in the laboratory. The results show that the key component temperature of CDC-MCSET is lower than that of T-MCSET. Therefore, the conduction loss, heating capacity, and damage rate of the key components are reduced. The service life of the components is extended, and the efficiency of MCSET is further improved.

d) The two linear relationships between input and output voltages and between input voltage and output current are analyzed in the controlled-source circuit. The contrast and fitting curves of these parameters are provided. CDC-MCSET demonstrates high fit and good external characteristics.

e) Saber simulation and MCSET are used in the laboratory to verify the conclusions. The experimental waveforms and analyses are provided. The developed marine electromagnetic detection system draws on the latest technology of switching power supply to obtain high stability, high linearity, high power density, and high transmission efficiency of MCSET. This work lays a solid foundation for further sea exploration, especially deep-sea exploration.

ACKNOWLEDGMENT

This work was supported by the Key Special Projects of Instruments and Technologies in the Deep Sea for the National Key R&D (Adaptive Closed Loop Constant Current Technology and Laboratory Experiment), Grant No. 2016YFC0303103.

REFERENCES

[1] S. Constable, "Ten years of marine CSEM for hydrocarbon exploration," *Geophysics*, Vol. 75, No. 5, pp.75A67-75A81, Sep./Oct. 2010.

[2] M. C. Sinha, P. D. Patel, M. J. Unsworth, T. R. E. Owen, and M. R. G. Maccormack, "An active source electromagnetic sounding system for marine use," *Marine Geophysical Res.*, Vol. 12, No. 1-2, pp. 59-68, 1990.

[3] S. Constable, and L. J. Srnka, "An introduction to marine controlled source electromagnetic methods for hydro-carbon exploration," *Geophysics*, Vol. 72, No. 2, pp. WA3-WA12, Mar./Apr. 2007.

[4] K. Weitemeyer, and S. Constable, "Navigating marine electromagnetic transmitters using dipole field geometry," *Geophysical Prospecting*, Vol. 62, No. 3, pp. 573-596, May 2014.

[5] S. Petersen, M. Hannington, T. Monecke, and G. Cherkashov, "Are modern seafloor massive sulfide deposits a possible resource for mankind: Lessons learned from shallow drilling operations," *Oceans'11 MTS/IEEE KONA*, pp. 1-3, 2011.

[6] D. Myer, S. Constable, and K. Key, "Broad-band waveforms and robust processing for marine CSEM surveys," *Geophysical Journal International*, Vol. 184, No. 2, pp. 689-698, Feb. 2011.

[7] A. Orange, K. Key, and S. Constable, "The feasibility of reservoir monitoring using time-lapse marine CSEM," *Geophysics*, Vol. 74, No. 2, pp. F21-F29, Mar./Apr. 2009.

[8] J.-G. Cho, J. A. Sabate, G. Hua, and F. C. Lee, "Zero-voltage and zero-current-switching full bridge PWM converter for high-power applications," *IEEE Trans. Power Electron.*, Vol. 11, No. 4, pp. 622-628, Jul. 1996.

[9] R. Redl, N. O. Sokal, and L. Balogh, "A novel soft-switching full-bridge DC/DC converter: analysis, design considerations, and experimental results at 1.5 kW, 100 kHz," *IEEE Trans. Power Electron.*, Vol. 6, No. 3, pp. 408-418, Jul. 1991.

[10] R. Redl, L. Balogh, and D. W. Edwards, "Optimum ZVS full-bridge DC–DC converter with PWM phase-shift control analysis design consideration and experimental results," in *Proc. APEC' 1994.* Vol. 1, pp. 159-165. 1994.

[11] X. Ruan and F. Liu, "An improved ZVS PWM full-bridge converter with clamping diodes," *2004 IEEE 35th Annual Power Electronics Specialists Conference*, Vol. 2, pp. 1476-1481, 2004.

[12] W. Chen, X. Ruan, Q. Chen, and J. Ge, "Zero-voltage-switching PWM full-bridge converter employing auxiliary transformer to reset the clamping diode current," *IEEE Trans. Power Electron.*, Vol. 25, No. 5, pp. 1149-1162, May. 2010.

[13] X. Wu, J. Zhang, X. Xie, and Z. Qian, "Analysis and optimal design considerations for an improved full bridge ZVS DC–DC converter with high efficiency," *IEEE Trans. Power Electron.*, Vol. 21, No. 5, pp. 1225-1234, Sep. 2006.

[14] H. Tao, Y. Zhang, and X. Ren, "Small-signal modeling of marine electromagnetic detection transmitter controlled-source circuit," *Mathematical Problems in Engineering*, pp. 1-9, 2015.

[15] H. Tao, Y. Zhang, and X. Ren, "A novel circuit of marine controlled source electromagnetic transmitter," *Electric Power Components and Systems*, Vol. 44, No. 9, pp. 1063-1070, 2016.

[16] F. Yu and Y. Zhang, "Modeling and control method for high-power electromagnetic transmitter power supplies," *J. Power Electron.*, Vol. 13, No. 4, pp. 679-691, Jul. 2013.

[17] S.-Y. Lin and C.-L. Chen, "Analysis and design for RCD clamped snubber used in output rectifier of phase-shift full-bridge ZVS converters," *IEEE Trans. Ind. Electron.*, Vol. 45, No. 2, pp. 358-359, Apr. 1998.

[18] L. H. Mweene, C. A. Wright, and M. F. Schlecht, "A 1 kW, 500 kHz front-end converter for a distributed power supply system," in *Proc .APEC' 89*, pp. 423-432, 1989.

[19] M. Xu, Y. Ren, J. Zhou, and F. C. Lee, "1-MHz self-driven ZVS full-bridge converter for 48-V power pod and DC/DC Brick," *IEEE Trans. Power Electron.*, Vol. 20, No. 5, pp. 997-1006, Sep. 2005.
[20] J. A. Sabaté, V. Vlatkovic, R. B. Ridley, F. C. Lee, and B. H. Cho, "Design considerations for high-voltage high-power full-bridge zero-voltage switched PWM converter," in *Proc. APEC' 90*, pp. 275-284, 1990.
[21] L. Zhao, H. Li, X. Wu, and J. Zhang, "An improved phase-shifted full-bridge converter with wide-range ZVS and reduced filter requirement," *IEEE Trans. Ind. Electron.*, Vol. 65, No. 3, pp. 2167-2176, Mar. 2018.
[22] J. Tian, J. Gao, and Y. Zhang, "Design of a novel integrated L-C-T for PSFB ZVS converters," *J. Power Electron.*, Vol. 17, No. 4, pp. 905-913, Jul. 2017.
[23] J. Tian, Y. Zhang, and X. Ren, "Calculation of leakage inductance of integrated magnetic transformer with separated secondary winding used in ZVS PSFB converter," *J. Magn.*, Vol. 21, No. 4, pp. 644-651, Dec. 2016.
[24] S. Liu, S. Wang, L. Wang, and H. Ben, "Analysis and control of parasitic oscillation of the output rectifier bridge in DC/DC converter," *Power Electronics of China*, Vol. 43, No. 10, pp. 83-85, Oct. 2009.

Hongxi Song was born in Henan, China, in 1986. He received his M.S. degree from Inner Mongolia University of Technology in 2014. He is currently working toward his Ph.D. degree at the Faculty of Information Technology, Beijing University of Technology, China. He participates in research activities dealing with marine controlled-source electromagnetic detection systems. His research interests include power electronics and electric drives, high-frequency switching power supplies, and Zigbee technology.

Yiming Zhang was born in Hubei, China, in 1964. He received his B.E. degree from the School of Electronic, Information and Electrical Engineering, Shanghai Jiao Tong University, Shanghai, China, in 1988 and his M.E. degree from the School of Electrical Engineering and Automation, Harbin Institute of Technology, Harbin, China, in 1992. From 2000 to 2007, he worked as a senior researcher in the Institute of Electrical Engineering, Chinese Academy of Sciences, Beijing, China. Since 2008, he has been a professor at the Faculty of Information Technology, Beijing University of Technology, China. His current research interests include intelligent power management, motor speed control, servo drives, and motor energy conservation.

Junxia Gao received her B.S. degree in automation from Taiyuan University of Technology, Taiyuan, China, in 2001, her M.S. degree in control theory and control engineering from Beijing University of Technology, Beijing, China, in 2004, and her D.S. degree in detection technology and automation from Beijing University of Technology, Beijing, China, in 2017. Presently, she is a teacher in the Faculty of Information Technology, Beijing University of Technology. Her research specialization is on low-field pulsed nuclear magnetic resonance techniques, electromagnetic theory and technology, and switching power supply.

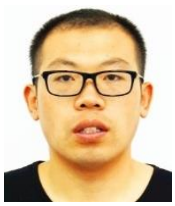

Yu Zhang was born in Hebei, China, in 1988. He received his M.S. degree in power electronics and power transmission from the North China University of Technology in 2016. He is currently working toward his Ph.D. degree at the Faculty of Information Technology, Beijing University of Technology, China. He participates in research activities dealing with the electromagnetic compatibility of electrical and electronic equipment. His research interests include power electronics and switching supply.

Xinyue Feng was born in Jilin, China, in 1993. She received her B.S. degree from Northeast Electric Power University in 2016. She is currently working toward her M.S. degree at the Faculty of Information Technology, Beijing University of Technology, China. She is participating in research activities dealing with marine controlled-source electromagnetic detection systems. Her current research interests include nuclear magnetic resonance technique, electromagnetic theory and technology, and switching power supply.